Physica Medica 65 (2019) 76–83

Contents lists available at ScienceDirect

Physica Medica

journal homepage: www.elsevier.com/locate/ejmp

Original paper

Attenuation correction of a flat table top for radiation therapy in hybrid PET/MR using CT- and ^{68}Ge/^{68}Ga transmission scan-based μ-maps

Stephan Witoszynskyj[a,1], Piotr Andrzejewski[b,c,1], Dietmar Georg[b,c], Marcus Hacker[a], Tufve Nyholm[d], Ivo Rausch[e], Barbara Knäusl[b,c,*]

[a] Division of Nuclear Medicine, Department of Biomedical Imaging and Image-Guided Therapy, Medical University of Vienna, Währingergürtel 18-20, 1090 Vienna, Austria
[b] Department of Radiotherapy, Comprehensive Cancer Center, Medical University of Vienna, Währingergürtel 18-20, 1090 Vienna, Austria
[c] Christian Doppler Laboratory for Medical Radiation Research for Radiation Oncology, Medical University of Vienna, Währingergürtel 18-20, 1090 Vienna, Austria
[d] Department of Radiation Sciences, Umeå University, SE-90187 Umeå, Sweden
[e] Center for Medical Physics and Biomedical Engineering, Medical University of Vienna, Währingergürtel 18-20, 1090 Vienna, Austria

ARTICLE INFO

Keywords:
Attenuation correction
PET/MR
μ-Map
Radiation oncology

ABSTRACT

Hybrid PET/MR offers new opportunities in radiation oncology for tissue/tumour characterisation and response assessment. Attenuation correction (AC) is an important issue especially in the presence of immobilization devices and flat table tops (FTT). The goal of this study was to compare two methods of AC using CT- and ^{68}Ge/^{68}Ga transmission scan-based attenuation maps (μ-maps) for a custom-designed FTT. Measurements were performed in the mMR PET/MR and TrueV PET/CT Biograph Siemens scanners with three different phantoms, namely the Siemens MR-QA, a cubic canister and the NEMA IEC body phantom. The study revealed that the MR image quality is not hampered by the presence of the FTT. For cubic canister applying the scanner's inherent AC alone resulted in inaccuracies in PET images, with up to −4.0% underestimation of the activity. The mean NEMA sphere activity measurements without FTT, agreed within 3.5% with the respective inserted activity. Placing the FTT in the PET/MR scanner resulted in a difference to the injected activity of 4.5% when the table was not corrected for. By introducing the μ-maps the discrepancy between the used activity and the measurements decreased down to 2.6%. To improve the AC of the FTT the creation of a dedicated μ-map was necessary while the CT-based μ-map performed equally good as the source transmission scan-based one.

1. Introduction

The potential of positron emission tomography (PET)/magnetic resonance (MR) hybrid scanners is currently explored in clinical studies. Various arguments are brought up as possible pros and cons of that new technology [1–6]. The direct comparison with PET/computed tomography (CT) or MR alone is difficult since the machines themselves are often equipped with different hardware and/or software solutions [7–10]. Radiation oncology (RO) is one of the fields that can benefit from such technology providing complementary information in many aspects [11–18]. It can be used for disease detection, target definition as well as treatment planning, treatment monitoring and response assessment [19–29].

The implementation of hybrid PET/MR scanners overcame the difficulty of PET-MR image registration necessary when using serial MR and PET/CT imaging. To fully exploit the benefits of the hybrid PET/MR imaging in RO some challenges have to be overcome. One of the most widely discussed issues is the correction for attenuation of the PET signal in the patient as well as in the scanner hardware components [26,30–41]. Many different approaches, often disease location dependent, are being tested and gradually commercially implemented for patient related attenuation correction (AC). Similarly, PET/MR vendors are taking care to adapt and design their hardware to minimize attenuation and to simplify the correction. In order to facilitate an accurate image fusion, the patient positioning and immobilization aids used daily in RO at the linear accelerator also need to be used while scanning and hence need to be taken into account in AC procedures.

Various systems and solutions are being used depending on the existing clinical needs and capabilities. Patients with different tumour indications are treated in different positions requiring varying aids like

* Corresponding author at: Department of Radiotherapy, Comprehensive Cancer Center, Medical University of Vienna, Währingergürtel 18-20, 1090 Vienna, Austria.
E-mail address: barbara.knaeusl@meduniwien.ac.at (B. Knäusl).
[1] Both authors contributed equally to this work.

https://doi.org/10.1016/j.ejmp.2019.08.005
Received 28 February 2019; Received in revised form 1 August 2019; Accepted 2 August 2019
Available online 19 August 2019

arm rests, knee rolls, neck pillows and head masks. Many of these have multiple shape options or are specifically customized to the patient's anatomy (moulds, thermoplastics, vacuum mattress etc.). For attenuation correction all the MR specific components like flexible RF coils, RF coil holders or body bridges need to be taken into account. Effects of these patient and MR system specific components on AC were already investigated by others [26,37]; consequently established correction procedures can be implemented at other institutions. A device that is always present for radiation oncology specific imaging, regardless of a treatment type and indication, is the flat table top (FTT) which can differ essentially in type and production material. A FTT is typical for RO and used to facilitate a reproducible patient's position during the treatment: at the stage of imaging for planning and dose delivery. Such tables need to meet requirements of three disciplines: nuclear medicine, MR imaging and radiation oncology; and respectively, cause as little attenuation and scattering as possible, be MR field neutral and be compatible with other positioning aids. Although these requirements are relatively easy to meet separately, all together they are a challenge when weight, size and easiness of use in clinical routine need to be taken into account.

A limited number of vendors offer custom-designed FTTs. The main goal of this study was to evaluate the impact of the purpose built FTT on the MR and PET image quality and activity quantification for the equipment available at the authors department. Since for objects containing higher attenuation values the CT-based attenuation correction may be insufficient [42–44] the second goal was to compare a CT- and a (^{68}Ge/^{68}Ga) transmission-based μ-map attenuation corrections.

2. Materials and methods

2.1. Scanners and respective equipment

A Biograph mMR PET/MR scanner (Siemens, Erlangen, Germany) along with a dedicated mMR PET/MR custom-designed flat table top (X-tend ApS, Hornslet, Denmark) was used in this study. The PET/MR system consists of a 3 T MR with a PET detector integrated in the magnet's bore allowing simultaneous PET and MR measurements. The PET detector is composed of 4 × 4 × 20 mm^3 LSO crystals which are read out by avalanche photodiodes (APD). The FTT is mountable on the top of the original mMR couch allowing the use of the spine array, body coil and all of the available surface coils.

Reference images were acquired with a Biograph TrueV PET/CT scanner (Siemens, Erlangen, Germany), while a GE Advance PET (GE Healthcare, Little Chalfont, United Kingdom) scanner equipped with ^{68}Ge/^{68}Ga sources was used for the acquisition of transmission scans.

The FTT with a weight of 15.8 kg consists of PA-GF30, fiber glass and polyactide and is 223 cm long (+2 cm for the handles) with a width of 56 cm. It is composed of 16 3D printed and injection moulded elements (14 elements of 14 cm length in the middle, one with 12.5 cm length at the bottom and one with 14.5 cm length at the top). Each of the central elements has 3 round fixation indexing slots (diameter of 28 mm) separated with a distance of 14 cm. It is compatible to various immobilization systems and equipped with semi-circular millings on both sides. The respective table features are presented in Fig. 1A-F.

The main plate has a thickness of 19 mm. The maximal thickness including diminutive assembly bolts that fasten the table in the mMR's rails is 34 mm. The effective shift of the table's surface position with regards to the original mMR table surface is 24 mm.

2.2. MR compatibility experiments

MR signal-to-noise ratio (SNR) measurements were performed using a 7.3 L spherical Siemens MR-QA phantom, filled with Bayol-Oil and Macrolex blue (Fig. 2A). It was positioned in the mMR scanner's magnetic isocenter with and without the FTT. The MR scans were repeated 10 times independently using the body coil integrated into the scanner's gantry with the following settings for each setup: TE 15 ms, TR 300 ms, matrix size 256 × 256, voxel size 1 × 1 × 5 mm^3, no acceleration. The SNR defined as $\frac{S_{mean}(AQ_{1-10})}{S_{SD}(AQ_{1-10})}$ was calculated voxelwise with a 3 × 3 × 3 averaging kernel, where $S_{mean}(AQ_{1\text{-}10})$ was the mean signal in acquisition 1 to 10, and $S_{SD}(AQ_{1\text{-}10})$ the respective standard deviation. The SNR was assessed in six regions of interest (ROIs) on the central slice of the phantom volume: one ROI with the diameter of the whole sphere and 5 smaller ROIs of 4 cm diameter placed in the centre, at the top, at the bottom as well as on the left and the right side of the phantom.

The MR B_o measurements were performed employing the same experimental setup as for the SNR measurements. A dual echo gradient recalled echo (GRE) series was acquired for each setup using the body coil with the following settings: TE 10.0/12.46 ms, TR 1000 ms, FA 90°, matrix of 128 × 128, voxel size of 2.3 × 2.3 × 5 mm^3, no acceleration. For a detailed analysis of the images frequency shift maps were calculated.

In order to assess the influence of the fixation slots of the FTT on the MR image, MR B_o measurements with the table were additionally acquired using 29 L cubic canister phantom (Fig. 2B) (filled with 3.6 g NaCl and 1.96 g $CuSO_4 \cdot 5H_2O$ per 1 liter of water). Two representative axial cross-sections were chosen for evaluation, one above the fixation slot and one above the solid table surface.

2.2.1. Generation of μ-maps

In the mMR scanner two types of μ-maps are used for attenuation correction. All standard elements of the PET/MR system that are fixed in a specific position during the scan (patient's table, coils, coil holders etc.) but "invisible" for the MR have their own μ-map provided by the vendor, called hardware μ-map. The attenuation caused by the patient itself, is corrected based on a μ-map generated from the acquired MR scan (MR μ-map) [39–41]. The MR μ-map is limited to the axial field of view (FOV) of the MR scan, whereas the hardware μ-maps cover the whole axial area within the gantry [42]. The μ-map that is ultimately used for the attenuation correction for a respective measurement is a sum of the hardware μ-map and the MR μ-map.

Two FTT μ-maps were generated and positioned accordingly in the coordinate system of mMR hardware μ-map (cf. Fig. 3):

- a CT-based μ-map was obtained from the acquired CT scans of four sections of the FTT (a Biograph TrueV PET/CT standard vendor supplied AC CT protocol: 120 kV, 295 mAs, matrix of 512 × 512 and voxel size of 1.37 × 1.37 × 5.0 mm^3, reconstruction kernel B19f). The resulting Hounsfield units (HU) were converted to linear attenuation coefficients (LAC) at 511 keV photons using the bilinear scaling method [45]. The volume was resampled to 1 × 1 × 1 mm^3 isotropic voxels and the resulting sub segment was duplicated to form a μ-map of the full FTT;
- a standard PET transmission scan-based μ-map was obtained on the GE Advance PET scanner having a 15.2 cm axial FoV using a transmission scan performed with the in-build ^{68}Ge/^{68}Ga sources. The FTT was positioned at the level of the scanner's isocenter. The scan was performed in high resolution mode. Five PET positions having three slices overlap were obtained. This resulted in a 3D volume of 163 slices. The scanning time was 1 hour per position. The images were reconstructed with a matrix size of 256 × 256 and voxel size 2.15 × 2.15 × 4.25 mm^3 using the filtered back projection with zeroth order Hanning filter with a cut-off of 4.3 mm. To compute the μ-map, the ^{68}Ge/^{68}Ga transmission images were first resampled to 1 × 1 × 1 mm^3 isotropic voxels. The data-set was reduced to the central four, 14 cm long elements, which were averaged to reduce noise. The outer slices were discarded to avoid the scanner's sensitivity drop offs at the edges. The resulting segment was duplicated to form a μ-map of the full FTT.

To position the generated FTT μ-maps in the coordinate system of

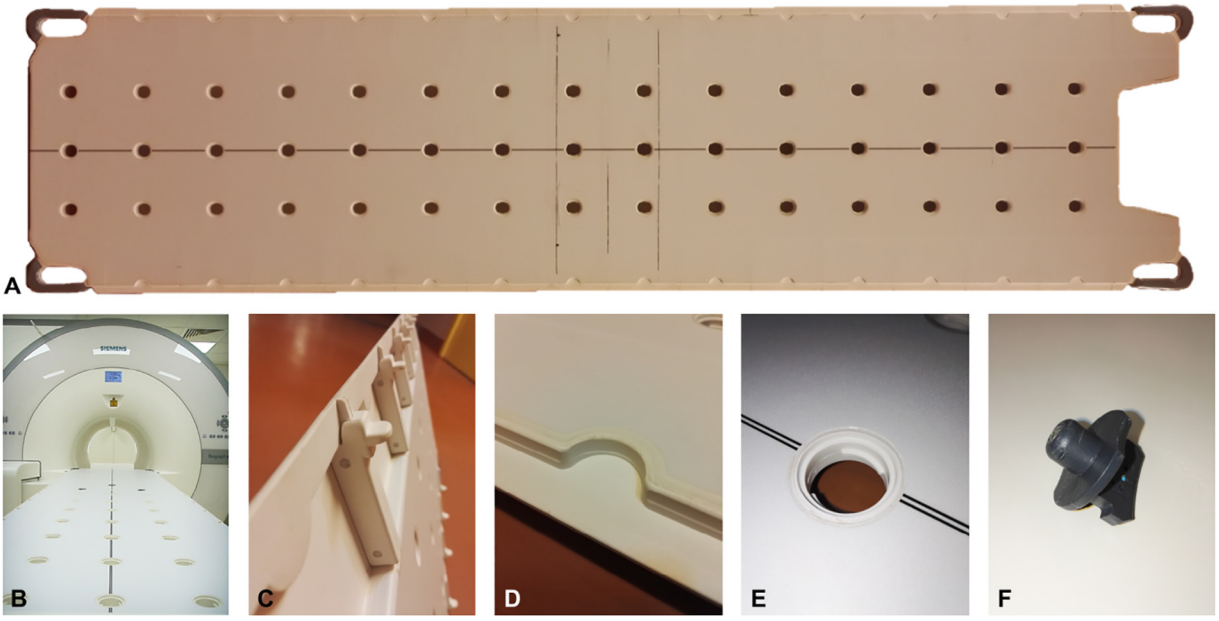

Fig. 1. A – FTT's view from the top; B – position in the PET/MR scanner; C – bottom view: assembly joints and setup guides; D and E – fixation and indexing slots; F – removable immobilization fixation bolts with MR and CT markers.

the hardware μ-maps, series of PET/MR and CT scans were performed. The mMR quality control ^{68}Ge rod sources (PET-281/1.4 MR, Sanders Medical, Knoxville, USA) positioned on the FTT were used to determine its surface. Spheres of 4 cm diameter, half-filled with saline solution of ^{18}F-FDG and MR contrast agent, were placed in the table's indexing slots. A CT scan of the table with the spheres was fused to the acquired PET/MR images as well as the generated μ-maps to serve as reference for positioning in the scanner's μ-maps coordinate systems.

2.3. Attenuation experiments

Both, the PET/CT and PET/MR scans were performed with and without presence of the FTT using two phantoms:

i. the NEMA IEC body phantom (6 fillable spheres of 28 mm inner diameter; without the lung insert; wall thickness: 3 mm) (Fig. 2C and supplementary Fig. A1) filled with ^{18}F-FDG, MR-contrast and saline aqueous solution (37.8 kBq/mL activity concentration, 0.2 mmol/L Gd-DO3A-butrol, 0.9% NaCl; activity ratio of 8:1 between spheres and background [BKG]);
ii. a thin-walled (0.7 mm) cubic canister phantom (Fig. 2B) filled with the same solution (4.5 kBq/mL activity concentration).

As the thick plastic walls of the NEMA phantom could not be taken into account by the MR-based attenuation correction [33], a dedicated μ-map was created in the same way as for the FTT (see Section 2.2.1). In order to concentrate on the influence of the FTT and not on the uncertainties introduced by the attenuation in the NEMA phantom, a CT based μ-map was used for all measurements. This was not necessary for the cubic canister phantom, because of its thin walls of only 0.7 mm.

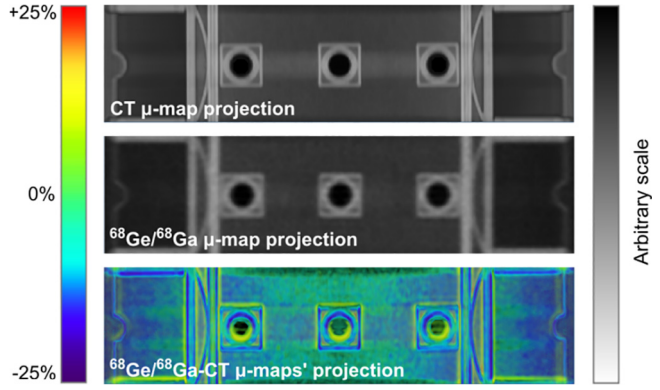

Fig. 3. FTT's CT-based μ-map orthogonal projection, ^{68}Ge/^{68}Ga transmission scan-based μ-map orthogonal projection and difference of the two in relative numbers.

The phantoms were positioned in the scanners' isocenter and the acquisition time was 10 min. The attenuation correction for PET/CT images was performed based on the CT data by default and for PET/MR images based on the manually generated μ-maps, namely CT- and ^{68}Ge/^{68}Ga transmission scan- based μ-maps created as described in

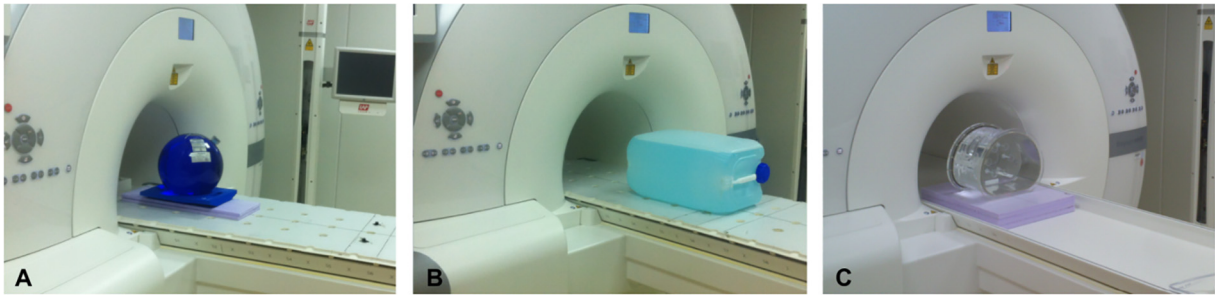

Fig. 2. Phantoms used for the tests: A – MR-QA phantom; B – canister phantom; C – customized NEMA phantom.

paragraph 2.2.1. For PET/MR reconstructions the NEMA phantom correction was based on both the MR μ-map and on the CT-based μ-map for comparison. All images were reconstructed with the OSEM reconstruction method with 4 iterations and 21 subsets employing a 5 mm Gaussian convolution kernel. For evaluation all measurements were corrected for decay.

PET phantom measurements were evaluated as follows:

2.3.1. NEMA phantom

- the variation of the activity measured in the NEMA phantom spheres was assessed as the $\frac{Max_{S1:S6} - Min_{S1:S6}}{Mean_{S1:S6}}$ of mean activity values; mean activity values were measured in the six, 15 mm diameter spherical ROIs placed in the center of each sphere (S1 to S6, cf. supplementary Fig. A1);
- the relative difference of the mean activity in the sphere (15 mm diameter ROI) and in the background regions was assessed as the difference between measurements with and without FTT normalized to the injected activity (done for different μ-maps and scanners); NEMA ROIs were grouped in pairs based on the distance to the FTT (cf. supplementary Fig. A1);

2.3.2. Canister phantom

- the anterior-posterior (A-P) and cranio-caudal (C-C) profiles were plotted and the uniformity index UI $\left(UI = 100\% \bullet ABS\left[\frac{MAX - MIN}{MAX + MIN}\right]\right)$ was assessed for the PET series of the canister phantom scanned in the PET/CT- and PET/MR with and without FTT, reconstructed using different AC μ-maps. The A-P profiles were plotted as the mean value over a 20 mm wide stripe in the center slice of the phantom and C-C profiles slice-wise as the mean over a 10 cm circular ROI placed in the center of the phantom. The UI was calculated on a 10 cm long axial, central part of the phantom excluding a 1 cm margin from the phantom wall and computed using a sliding window approach with a 5 × 5 voxel ROI (volume of 0.8 cc) on a slice-by-slice basis.

3. Results

3.1. MR compatibility experiments

No differences between SNR images acquired with and without FTT were detected. The mean SNR value at the slice through the centre of the phantom was 98.0 ± 27.1 with FTT and 98.3 ± 27.0 without FTT. Furthermore, all SNR values measured in five smaller ROIs were comparable without a statistically significant difference: ROI_{top}- 103.1 and 102.1, ROI_{bottom}- 98.9 and 99.5, ROI_{centre}- 95.9 and 95.3, ROI_{left}- 93.9 and 94.0, ROI_{right}- 95.4 and 95.6.

The MR B_0 measurements of the MR-QA phantom with and without FTT revealed an insignificant, up to 10 Hz, increase in the frequency shift distribution histogram values measured at the slice through the centre of the phantom (Fig. 4).

The MR B_0 measurement with the canister phantom at the level of the indexing slots resulted in positive frequency shifts at the corners of the phantom most distant from the FTT (up to +78 Hz) and negative frequency shifts (up to −67 Hz) in proximity to the slots. Shifts not higher than ± 25 Hz were detected on the slices covering only the solid table surface, without any fixation slots.

3.2. μ-Maps

The materials composing the table resulted in HU ranging from about −1000 to +1000, with the median value of around −750 HU (Fig. 5), hence it was not necessary to apply the correction of the conversion as proposed by Paulus et al. [42].

3.3. Attenuation experiments

The differences between activities measured in the respective NEMA phantom spheres for PET/CT and PET/MR series with and without FTT using various combinations of μ-maps for AC are presented in Table 1.

The relative differences in the mean activity measured over all spheres and background regions for PET/CT and PET/MR series with and without FTT using various FTT μ-maps for AC are presented in Table 2.

The images resulting from the reconstructions of the canister and NEMA phantoms' PET scans using the different μ-maps are presented in Figs. 6 and 7, respectively.

Fig. 8 shows the A-P and C-C profiles of the canister phantom PET/CT- and PET/MR-PET scans with and without FTT, reconstructed using different AC μ-maps. The presence of the FTT, when corrected for, caused overestimation of the activity measured for both PET/CT and PET/MR series with respect to the measurement without the FTT. Based on the C-C profile analysis of the PET/MR image the overestimation (3.4 and 2.5)% was on average higher when the CT-based μ-map was used instead of the $^{68}Ge/^{68}Ga$ transmission scan-based one. Not correcting for the FTT in the PET/MR causes up to −4.0% underestimation of the activity. A rapid increase of that activity underestimation can also be observed on the A-P profiles, starting approximately 10 cm above the FTT surface (cf. dotted line on Fig. 8B). In the close proximity of the FTT the profiles on the images with and without FTT overlap less than further away from it. It is most pronounced for the non-corrected scenario, but can be seen for all other scenarios as well.

The evaluation of the canister phantom images revealed a UI of (16.7 ± 1.7)% for PET/CT without FTT and (26.3 ± 2.2)% for PET/CT with FTT. The UI for the PET/MR without FTT was (32.8 ± 3.0)%. Introduction of the FTT into the PET/MR and not correcting for its attenuation resulted in the UI of (53.3 ± 2.5)%. The AC using the CT-based and $^{68}Ge/^{68}Ga$ transmission scan-based μ-maps recovered the UI to (35.0 ± 2.8)% and (34.8 ± 2.7)%, respectively. The above mentioned UI differences can be observed in Fig. 6.

4. Discussion

Several groups investigated the need and solutions for attenuation correction of the hardware components in the PET/MR imaging [26,31,33,37,46–51]. Both, the MR and PET image quality and the true representation of the imaged objects have been investigated to assess the impact of the positioning and immobilization devices as well as receiving coils and coil holders. In this study a custom designed FTT was tested for its MR compatibility and two different approached for its AC were evaluated.

The FTT has shown to be fully MR-compatible. No image quality loss was observed and the measured frequency shifts were smaller than the receiver bandwidth. However, due to the change of the imaging geometry by introducing the FTT (e.g. the distance between patient and the spine coil increased by 24 mm) the image quality may degrade in certain clinical settings.

The generation of the μ-map based on the $^{68}Ge/^{68}Ga$ transmission scan was more cumbersome than the CT-based one. Due to the low activity of the used $^{68}Ge/^{68}Ga$ sources the process required more time than in the CT scanner and the image handling was more laborious. Due to the low resolution and the limited FOV, the $^{68}Ge/^{68}Ga$ transmission scans required additional processing and were difficult to position in the PET/MR's scanner frame of reference, which is essential for accurate AC.

The mean NEMA sphere activity values from both, attenuation corrected PET/CT and PET/MR measurements without FTT, agreed within 3.5% with the respective inserted activity (c.f. Table 1). Placing the FTT in the PET/MR scanner disturbed the PET measurement resulting in a difference to the true activity of 4.5% when the table was not corrected for. By introducing the μ-maps AC the discrepancy

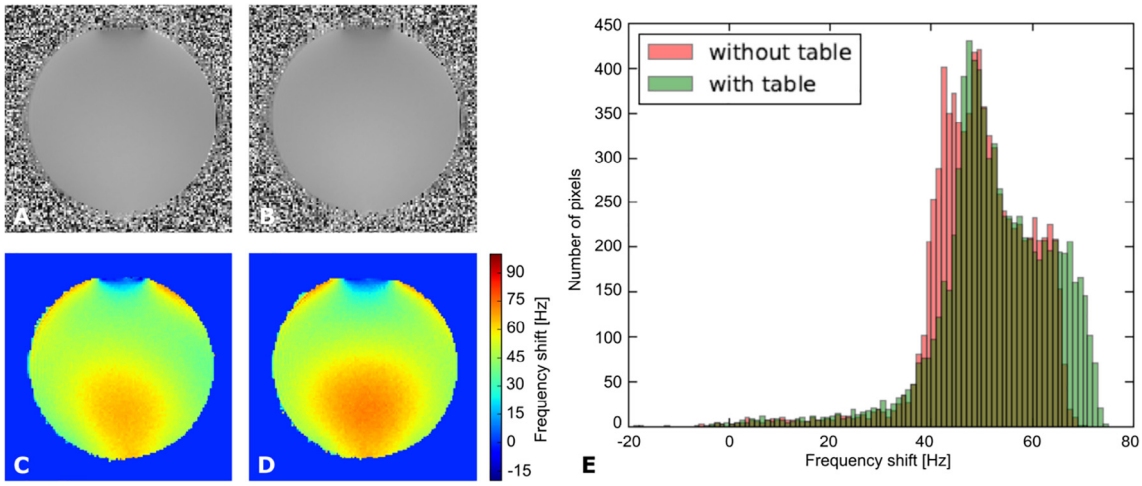

Fig. 4. A and B – images of the MR B_0 measurements of the MR-QA phantom with (A) and without (B) FTT; C and D – frequency shift maps [Hz] for the with (C) and without (D) FTT; E – frequency shift distribution histogram with (green) and without (pink) FTT.

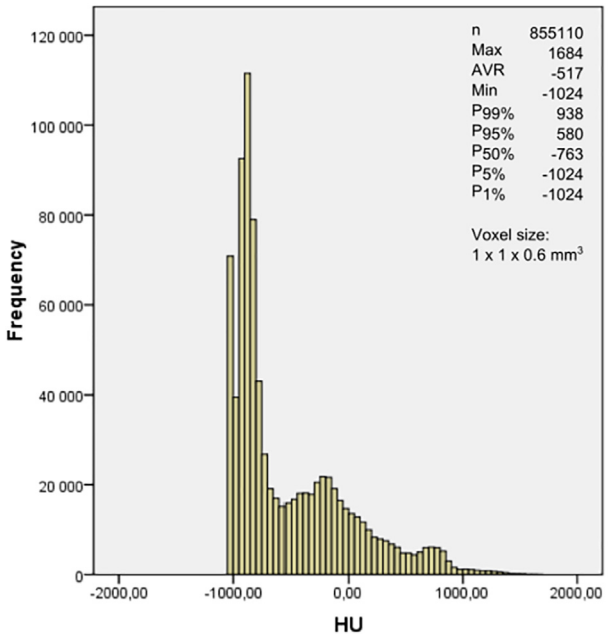

Fig. 5. Distribution of HU in the CT scan of the FTT. It includes the air that is in the indexing holes (ROI defined at the border of the table).

between the used activity and the measurements decreased down to 2.6 and 2.8% for the ^{68}Ge/^{68}Ga transmission scan-based and CT-based correction, respectively (c.f. Table 1).

The evaluation of the relative differences between the measurements performed with and without FTT showed that even for the PET/CT reference experiment, the introduction of the table into the scanner's gantry caused up to 3.2% difference for the spheres positioned closest to the table (cf. Table 2 and supplementary Fig. A1).

For the background regions the overestimation of the measured activity reached 10.1% at 2 cm distance from the FTT's surface. The background activity between the NEMA spheres was different by 19.1%. Not correcting for the FTT in the PET/MR caused an underestimation of the measured activity in all considered background regions. Correcting inverted the effect and moved the results towards the values resulting from the PET/CT experiment. Although the average over all spheres was closer to the reference measurement than for PET/CT the SD was higher and the results depend on the position of the sphere. The discrepancy for the regions BKG_{1-3} was smaller than for

Table 1
Variation between the activity measured in the respective NEMA phantom spheres, assessed as the $\frac{Max_{S1:S6} - Min_{S1:S6}}{Mean_{S1:S6}}$ of mean values measured in the 15 mm diameter spherical ROIs placed in the centre of each sphere. Measurements were reconstructed with different combinations of FTT and NEMA phantom μ-maps (CT-based, ^{68}Ge/^{68}Ga transmission scan- based, MR-based, no – no μ-map used, n/a – no FTT was used).

	FTT μ-map	NEMA phantom μ-map	"Activity variation" in 15 mm spheres
			PET/CT
No FTT	n/a	CT	3.5%
With FTT	CT	CT	5.0%
			PET/MR
No FTT	n/a	MR	8.0%
No FTT	n/a	CT	3.5%
With FTT	no	CT	4.5%
With FTT	^{68}Ge/^{68}Ga	CT	2.6%
With FTT	CT	CT	2.8%

PET/CT, but the activity overestimation is higher close to the table surface (c.f. Table 2).

Figs. 6 and 7 visualize the effect of the FTT on the PET images of the canister and the NEMA phantom acquired with PET/CT and PET/MR scanner. For PET/CT it is almost impossible to recognize the difference by visual inspection, while for PET/MR the uncorrected images are clearly showing the underestimation of the activity in the close proximity of the table. For the images reconstructed with the generated μ-maps the image quality is restored. An increase of the measured activity in the central part of the canister phantom, which is also visible at the A-P profile (Fig. 8A), could be explained by the underestimation of the scatter effects in the PET/MR reconstruction, which was also observed for the NEMA spheres (Table 1).

To our knowledge the scatter correction induced overestimation of the activity was not yet reported and is also revealed by the lack of flatness of the PET/MR profiles. Paulus et al. [26] performed similar experiments with a big water-filled round and symmetric phantom but in another measurement geometry. The related profiles were determined in C–C direction and the ROIs placed in the phantom were large or a mean value over several ROIs was calculated, hence this overestimation was not detected. The central brightening effects on MR images of large water-filled phantoms occur due to the high dielectric constant of water reducing the RF excitation wavelength and resulting in standing RF waves [51,52]. That however has no influence on the MR μ-map of the phantom's content, since the scanner segments only 3

Table 2
Relative differences in the mean activity measured over all NEMA phantom spheres (15 mm diameter ROI) and background regions between measurements with and without FTT (normalized to the used activity) for different μ-maps. Spheres and background ROIs were grouped in pairs based on the distance to the FTT. Abbreviations: FTT – flat table top; S_x – sphere number x; SD – standard deviation; BKG_x – background area number x; shares and background areas naming as in Supplementary Fig. A1.

FTT μ-map	$S_{1\&2}$	$S_{3\&4}$	$S_{5\&6}$	Mean	SD	$BKG_{1\&2}$	BKG_3	$BKG_{2\,cm}$	Mean	SD
					PET/CT					
CT	2.6%	1.0%	3.2%	2.3%	1.2%	9.1%	19.1%	10.1%	12.7%	4.5%
					PET/MR					
No	−11.0%	−7.9%	−7.1%	−8.7%	2.1%	−7.8%	−7.2%	−7.0%	−7.3%	0.4%
^{68}Ge/^{68}Ga	−4.6%	1.0%	3.7%	0.0%	3.6%	1.8%	5.3%	13.4%	6.8%	4.9%
CT	−3.8%	2.1%	5.2%	1.2%	3.9%	2.9%	6.8%	16.2%	8.7%	5.6%

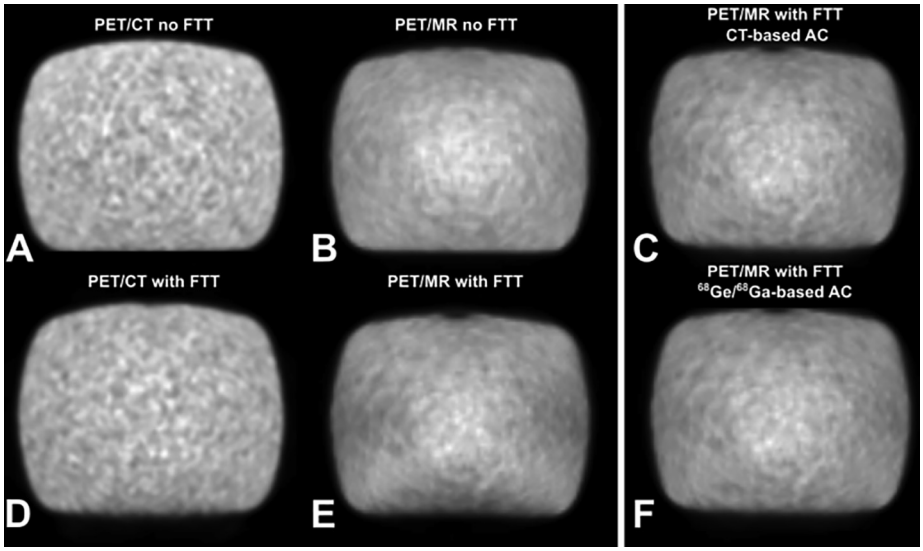

Fig. 6. PET images of the canister phantom: A and D – acquired in the PET/CT without and with the FTT; B and E – acquired in the PET/MR without and with the FTT not correcting for attenuation in the FTT; C and F – acquired in the PET/MR with the FTT using CT-based and ^{68}Ge/^{68}Ga transmission scan-based μ-maps for AC, respectively.

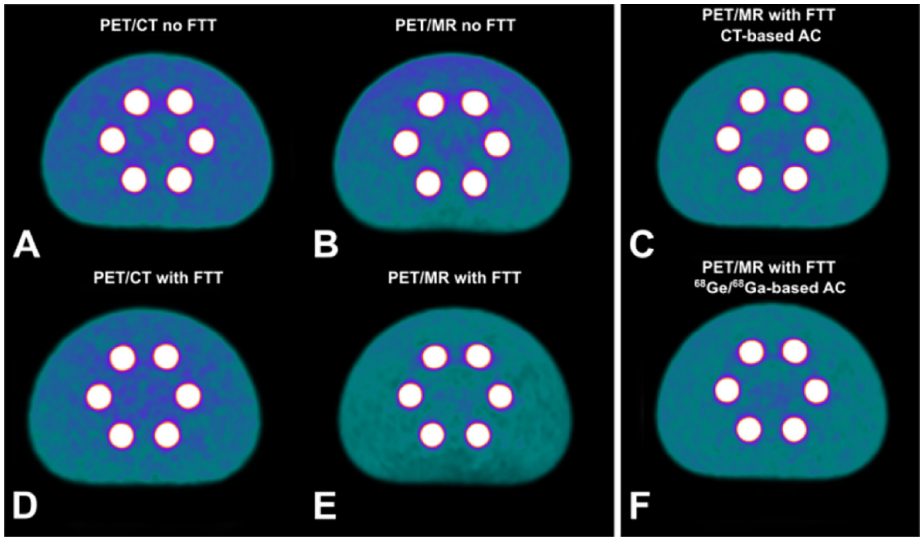

Fig. 7. PET images of the NEMA phantom: A and D – acquired in the PET/CT without and with the flat table top; B and E – acquired in the PET/MR without and with the flat table top not correcting for attenuation in the FTT; C and F – acquired in the PET/MR with the flat table top using CT-based and ^{68}Ge/^{68}Ga transmission scan-based μ-maps for AC, respectively.

types of materials: water, fat and air. On the other hand, the presence of photopenic effects (halo-artefacts) was previously reported and improper scatter correction was found to be the potential source of error [53].

The comparison of the C-C profiles along the z-axis of the cylinder phantom (cf. Fig. 8C) with the results of Paulus et al. [26], who assessed the influence of another FTT on the PET/MR imaging, is affirmative. The relative difference in measured activity between the reference scan without and the scan with FTT, reached on average −4.0% in the current study and −3.8% in [26]. Using dedicated ^{68}Ge/^{68}Ga transmission scan- and CT-based μ-maps overestimated the activity from 2.5 to 3.4% whereas in [26] it caused underestimation of −0.6%. The slight differences can be the result of the different FTT, phantom, size of ROIs and geometry. In the presented study the ROI, based on which the profiles are plotted, was smaller and the phantom was positioned closer to the FTT surface.

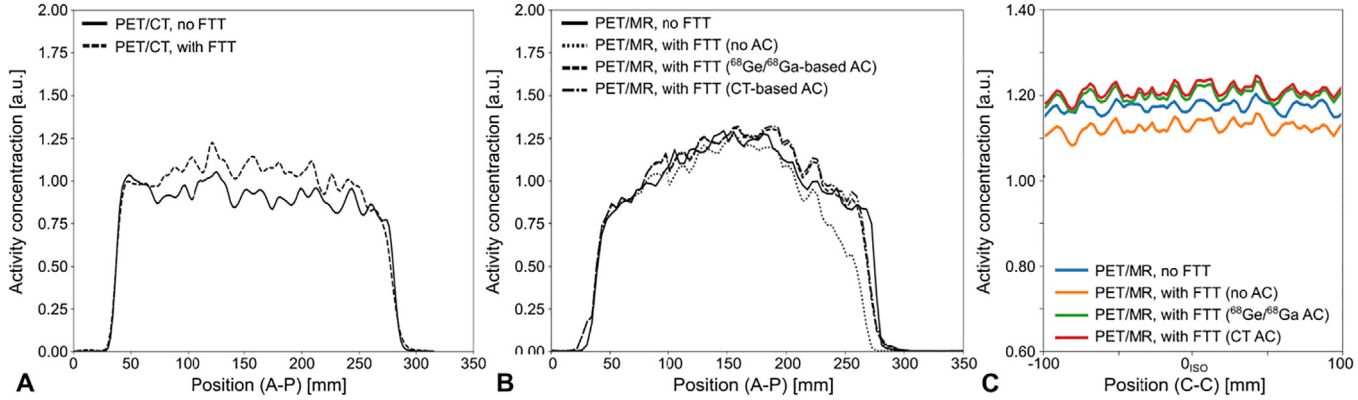

Fig. 8. A-P profiles of the canister phantom PET/CT- (A) and PET/MR- (B) PET series without and with FTT (for B reconstructed using different AC μ-maps); C – C–C profiles of the canister phantom PET/MR- PET series without and with flat table top reconstructed using different AC μ-maps.

The inclusion of the FTT's μ-map is an off-line process that has to be conducted by the expert personnel. An automatic recognition of the table by the scanner would be a major improvement of the clinical workflow and a reduction of the risk not including the FTT in the AC. The respective μ-map could be delivered together with the hardware to assure correct and uniform use among different facilities. Such a solution is already implemented for the coils that are used during the scan.

In the clinical environment the easy handling of medical equipment (e.g. positioning aids) plays a pivotal role. It assures the correct usage, decreases the procedure time (and cost) as well as assures patients' safety and comfort. The small gantry diameter of the PET/MR scanner can be a limiting factor for the usage of some of the typical RO-specific positioning aids. The tested FTT is a good alternative to the standard non-MR compatible RO-specific positioning aids as it holds in its setup position, is thin, stiff, and easy to handle and sterilize.

The construction of the FTT, with its extensive number of indexing slots, was recognized as a possible cause of false activity reconstruction in the proximity of the slots. Additional series of profiles were evaluated both through the centre of the hole and its edge (canister phantom experiment). These profiles revealed that the differences were higher for the CT-based μ-map and were mostly pronounced outside of the relevant field of view (below of the FTT's surface). Within the phantom's volume, the artefacts causing errors of about ± 15 % were only detectable up to 1.5 cm above the FTT's surface.

One limitation in this study is the fact that the AC method in the PET/CT could not be influenced to explore the replacement of the FTT CT image with its transmission μ-map. Furthermore, there are differences between the reconstruction process between PET/CT and PET/MR which are related to the attenuation and scatter correction algorithms implemented by the vendor and not changeable by the user [48,54].

The exclusive focus of our study on the FTT might be seen as another limitation. Besides the FTT, most other immobilization devices are indication specific and were partly investigated by other groups. For example, Paulus et al. investigated flexible RF coils, coil holders and body bridges for the same hybrid scanner system as used in the present study [26,49]. For clinical radiotherapy motivated imaging applications the authors combined these system specific results with the FTT results described in this manuscript.

The attenuation of immobilisation devices for the pelvic area, as e.g. needed for tumour biology studies in cervix cancer, is less explored, however currently under investigation by the authors. Including these aspects would go beyond the scope of the current study.

5. Conclusion

The MR image quality is not hampered by the presence of the FTT custom constructed from a specific MR-compatible composition of materials. Since the table is not taken into account in the scanners automatic attenuation correction the measured activity represented on PET images is inaccurate. In order to achieve PET images comparable to the clinical standard defined by the PET/CT, the attenuation correction in the mMR scanner has to be improved by implementing a dedicated table hardware μ-map. In the frame of this study a transmission scan as well as a CT-based μ-map were created and included in the mMR scanner attenuation protocol. Although the transmission scan based μ-map is favourable due to the physical principle, the results revealed no significant difference between the two hardware μ-maps. Since PET scanners with transmission sources are not widely accessible anymore, the μ-map, once acquired, could be provided by the vendor together with the table. For tables build of materials of higher density the need for correction of the HU to PET LAC, as proposed by Paulus et al. [42] should be considered.

Declaration of Competing Interest

The authors declare that they have no known competing financial interests or personal relationships that could have appeared to influence the work reported in this paper.

Acknowledgements

The financial support by the Federal Ministry of Science, Research and Economy and the National Foundation for Research, Technology and Development (CD10277401) is gratefully acknowledged.

Appendix A. Supplementary data

Supplementary data to this article can be found online at https://doi.org/10.1016/j.ejmp.2019.08.005.

References

[1] Bailey DL, Pichler BJ, Gückel B, Barthel H, Beer AJ, Bremerich J, et al. Combined PET/MRI: Multi-modality Multi-parametric Imaging Is Here: Summary Report of the 4th International Workshop on PET/MR Imaging; February 23–27, 2015, Tübingen, Germany. Mol Imaging Biol 2015;17:595–608. https://doi.org/10.1007/s11307-015-0886-9.

[2] Bailey DL, Barthel H, Beyer T, Boellaard R, Gückel B, Hellwig D, et al. Summary report of the first international workshop on PET/MR imaging, March 19–23, 2012, Tübingen, Germany. Mol Imaging Biol 2013;15:361–71. https://doi.org/10.1007/s11307-013-0623-1.

[3] Bailey DL, Barthel H, Beuthin-Baumann B, Beyer T, Bisdas S, Boellaard R, et al. Combined PET/MR: Where are we now? Summary report of the Second International Workshop on PET/MR Imaging April 8–12, 2013, Tübingen, Germany. Mol Imaging Biol 2014;16:295–310. https://doi.org/10.1007/s11307-014-0725-4.

[4] Bailey DL, Pichler BJ, Gückel B, Barthel H, Beer AJ, Botnar R, et al. Combined PET/MRI: from Status Quo to Status Go. Summary Report of the Fifth International Workshop on PET/MR Imaging; February 15-19, 2016; Tübingen, Germany. Mol

Imaging Biol 2016;18:637–50. https://doi.org/10.1007/s11307-016-0993-2.
[5] Bailey DL, Antoch G, Bartenstein P, Barthel H, Beer AJ, Bisdas S, et al. Combined PET/MR: The Real Work Has Just Started. Summary Report of the Third International Workshop on PET/MR Imaging; February 17–21, 2014, Tübingen, Germany. Mol Imaging Biol 2015;17:297–312. https://doi.org/10.1007/s11307-014-0818-0.
[6] Herzog H, Pietrzyk U, Shah NJ, Ziemons K. The current state, challenges and perspectives of MR-PET. Neuroimage 2010. https://doi.org/10.1016/j.neuroimage.2009.10.036.
[7] Georg P, Andrzejewski P, Baltzer P, Daniel M, Wadsak W, Mitterhauser M, et al. Changes in Tumor Biology During Chemoradiation of Cervix Cancer Assessed by Multiparametric MRI and Hypoxia PET. Mol Imaging Biol 2017. https://doi.org/10.1007/s11307-017-1087-5.
[8] Daniel M, Andrzejewski P, Sturdza A, Majercakova K, Baltzer P, Pinker K, et al. Impact of hybrid PET/MR technology on multiparametric imaging and treatment response assessment of cervix cancer. Radiother Oncol 2017;125. https://doi.org/10.1016/j.radonc.2017.10.036.
[9] Sawicki LM, Grueneisen J, Schaarschmidt BM, Buchbender C, Nagarajah J, Umutlu L, et al. Evaluation of ^{18}F-FDG PET/MRI, ^{18}F-FDG PET/CT, MRI, and CT in whole-body staging of recurrent breast cancer. Eur J Radiol 2016;85:459–65. https://doi.org/10.1016/j.ejrad.2015.12.010.
[10] Spick C, Herrmann K, Czernin J. 18F-FDG PET/CT and PET/MRI perform equally well in cancer: evidence from studies on more than 2,300 patients. J Nucl Med 2016;57(3):420–30. https://doi.org/10.2967/jnumed.115.158808.
[11] Schaarschmidt BM, Heusch P, Buchbender C, Ruhlmann M, Bergmann C, Ruhlmann V, et al. Locoregional tumour evaluation of squamous cell carcinoma in the head and neck area: a comparison between MRI, PET/CT and integrated PET/MRI. Eur J Nucl Med Mol Imaging 2016;43:92–102. https://doi.org/10.1007/s00259-015-3145-z.
[12] Eiber M, Weirich G, Holzapfel K, Souvatzoglou M, Haller B, Rauscher I, et al. Simultaneous68Ga-PSMA HBED-CC PET/MRI Improves the Localization of Primary Prostate Cancer. Eur Urol 2016;70:829–36. https://doi.org/10.1016/j.eururo.2015.12.053.
[13] Sotoudeh H, Sharma A, Fowler KJ, McConathy J, Dehdashti F. Clinical application of PET/MRI in oncology. J Magn Reson Imaging 2016;44:265–76. https://doi.org/10.1002/jmri.25161.
[14] Fraum TJ, Fowler KJ, McConathy J, Parent EE, Dehdashti F, Grigsby PW, et al. PET/MRI for the body imager: abdominal and pelvic oncologic applications. Abdom Imaging 2015;40:1387–404. https://doi.org/10.1007/s00261-015-0390-3.
[15] Lindenberg L, Ahlman M, Turkbey B, Mena ECP. Advancement of MR and PET/MR in prostate cancer. Semin Nucl Med 2016:536–43.
[16] Freitag MT, Radtke JP, Hadaschik BA, Kopp-Schneider A, Eder M, Kopka K, et al. Comparison of hybrid 68Ga-PSMA PET/MRI and ^{68}Ga-PSMA PET/CT in the evaluation of lymph node and bone metastases of prostate cancer. Eur J Nucl Med Mol Imaging 2016;43:70–83. https://doi.org/10.1007/s00259-015-3206-3.
[17] Deuschl C, Kirchner J, Poeppel TD, Schaarschmidt B, Kebir S, El Hindy N, et al. ^{11}C-MET PET/MRI for detection of recurrent glioma. Eur J Nucl Med Mol Imaging 2018;45(4):593–601. https://doi.org/10.1007/s00259-017-3916-9.
[18] Grueneisen. Positron emission tomography/magnetic resonance imaging for local tumor staging in patients with primary breast cancer. Invest Radiol 2015;50:1–9. https://doi.org/10.1097/RLI.0000000000000197.
[19] Paulino AC, Thorstad WL, Fox T. Role of fusion in radiotherapy treatment planning. Semin Nucl Med 2003. https://doi.org/10.1053/snuc.2003.127313.
[20] Thorwarth D, Leibfarth S, Mönnich D. Potential role of PET/MRI in radiotherapy treatment planning. Clin Transl Imaging 2013. https://doi.org/10.1007/s40336-013-0006-2.
[21] Thorwarth D, Geets X, Paiusco M. Physical radiotherapy treatment planning based on functional PET/CT data. Radiother Oncol 2010. https://doi.org/10.1016/j.radonc.2010.07.012.
[22] Thorwarth D. Functional imaging for radiotherapy treatment planning: current status and future directions — a review. Br J Radiol 2015;88:20150056. https://doi.org/10.1259/bjr.20150056.
[23] Thorwarth D, Notohamiprodjo M, Zips D, Müller AC. Personalized precision radiotherapy by integration of multi-parametric functional and biological imaging in prostate cancer: a feasibility study. Z Med Phys 2015;27:21–30. https://doi.org/10.1016/j.zemedi.2016.02.002.
[24] Leibfarth S, Mönnich D, Welz S, Siegel C, Schwenzer N, Schmidt H, et al. A strategy for multimodal deformable image registration to integrate PET/MR into radiotherapy treatment planning. Acta Oncol (Madr) 2013;52:1353–9. https://doi.org/10.3109/0284186X.2013.813964.
[25] van der Heide UA, Houweling AC, Groenendaal G, Beets-Tan RGH, Lambin P. Functional MRI for radiotherapy dose painting. Magn Reson Imaging 2012;30:1216–23. https://doi.org/10.1016/j.mri.2012.04.010.
[26] Paulus DH, Thorwath D, Schmidt H, Quick HH. Towards integration of PET/MR hybrid imaging into radiation therapy treatment planning. Med Phys 2014;41:72505. https://doi.org/10.1118/1.4881317.
[27] Kuess P, Andrzejewski P, Nilsson D, Georg P, Knoth J, Susani M, et al. Association between pathology and texture features of multi parametric MRI of the prostate. Phys Med Biol 2017;62. https://doi.org/10.1088/1361-6560/aa884d.
[28] Edmund JM, Nyholm T. A review of substitute CT generation for MRI-only radiation therapy. Radiat Oncol 2017;12:1–15. https://doi.org/10.1186/s13014-016-0747-y.
[29] Karlsson M, Karlsson MG, Nyholm T, Amies C, Zackrisson B. Dedicated magnetic resonance imaging in the radiotherapy clinic. Int J Radiat Oncol Biol Phys 2009;74:644–51. https://doi.org/10.1016/j.ijrobp.2009.01.065.
[30] Martinez-Möller A, Souvatzoglou M, Delso G, Bundschuh RA, Chefd'hotel C, Ziegler SI, et al. Tissue classification as a potential approach for attenuation correction in whole-body PET/MRI: evaluation with PET/CT data. J Nucl Med 2009;50:520–6. https://doi.org/10.2967/jnumed.108.054726.
[31] Delso G, Martinez-Oller A, Bundschuh RA, Ladebeck R, Candidus Y, Faul D, et al. Evaluation of the attenuation properties of MR equipment for its use in a whole-body PET/MR scanner. Phys Med Biol 2010;55:4361–74.
[32] Hofmann M, Bezrukov I, Mantlik F, Aschoff P, Steinke F, Beyer T, et al. MRI-based attenuation correction for whole-body PET/MRI: quantitative evaluation of segmentation-and atlas-based methods. J Nucl Med 2011;52:1392–9. https://doi.org/10.2967/jnumed.110.078949.
[33] Ziegler S, Jakoby BW, Braun H, Paulus DH, Quick HH. NEMA image quality phantom measurements and attenuation correction in integrated PET/MR hybrid imaging. EJNMMI. Physics 2015;2. https://doi.org/10.1186/s40658-015-0122-3.
[34] Bezrukov I, Mantlik F, Schmidt H, Schölkopf B, Pichler BJ. MR-based PET attenuation correction for PET/MR imaging. Semin Nucl Med 2013. https://doi.org/10.1053/j.semnuclmed.2012.08.002.
[35] Wollenweber SD, Delso G, Deller T, Goldhaber D, Hüllner M, Veit-Haibach P. Characterization of the impact to PET quantification and image quality of an anterior array surface coil for PET/MR imaging. Magn Reson Mater Physics, Biol Med 2014;27:149–59. https://doi.org/10.1007/s10334-013-0388-1.
[36] Cho I, Kong E, Chun K. Image artifacts from MR-based attenuation correction in dedicated PET/MR breast coil for PET/MR mammography. Cho Al EJNMMI Phys 2015;2:17–21. https://doi.org/10.1186/2197-7364-2-S1-A62.
[37] Paulus D, Quick H. Hybrid positron emission tomography/magnetic resonance imaging. Invest Radiol 2016;51:624–34. https://doi.org/10.1097/RLI.0000000000000289.
[38] Eldib M, Bini J, Robson P, Calcagno C, Faul D, Tsoumpas C, et al. Markless attenuation correction for carotid MRI surface receiver coils in combined PET/MR imaging. Phys Med Biol 2015;60:4705–17. https://doi.org/10.3109/10253890.2015.1094689.Post-Traumatic.
[39] Fenchel M. Biograph mMR support of customer defined hardware μ-maps white-paper. Siemens Healthc AG 2011. PLM0077-G:1–11.
[40] Koesters T, Laforest R, Faul D. Customer documentation e7-tools for siemens biograph mMR SW version VA20. Siemens Healthc AG 2014:1–17.
[41] Quick HH. Integrated PET/MR. J Magn Reson Imaging 2014. https://doi.org/10.1002/jmri.24523.
[42] Paulus D, Tellmann Quick. Towards improved hardware component attenuation correction in PET/MR hybrid imaging. Phys Med Biol 2013;58:8021. https://doi.org/10.1088/0031-9155/58/22/8021.
[43] Tellmann L, Quick HH, Bockisch A, Herzog H. Beyer TT. The effect of MR surface coilson PET quantification in whole-body PET/MR: results from a pseudo-PET/MR phantom study. Med. Phys. 2011;38:2795–805.
[44] MacDonald LR, Kohlmyer S, Liu C, Lewellen TK, Kinahan PE. Effects of MR surface coils on PETquantification. Med. Phys. 2011;38:2948–56.
[45] Carney JPJ, Townsend DW, Rappoport V, Bendriem B. Method for transforming CT images for attenuation correction in PET/CT imaging. Med Phys 2006;33:976–83. https://doi.org/10.1118/1.2174132.
[46] Kartmann R, Paulus DH, Braun H, Aklan B, Ziegler S, Navalpakkam BK, et al. Integrated PET/MR imaging: Automatic attenuation correction of flexible RF coils. Med Phys 2013;40. https://doi.org/10.1118/1.4812685.
[47] Eldib M, Bini J, Calcagno ÞC, Robson PM, Mani V, Fayad ZA. Attenuation correction for flexible magnetic resonance coils in combined magnetic resonance/positron emission tomographic. Imaging 2013;49.
[48] Delso G, Fürst S, Jakoby B, Ladebeck R, Ganter C, Nekolla SG, et al. Performance Measurements of the Siemens mMR Integrated Whole-Body PET/MR Scanner n.d. doi: 10.2967/jnumed.111.092726.
[49] Paulus DH, Oehmigen M, Grüneisen J, Umutlu L, Quick HH. Whole-body hybrid imaging concept for the integration of PET/MR into radiation therapy treatment planning. Phys Med Biol 2016;61:3504–20. https://doi.org/10.1088/0031-9155/61/9/3504.
[50] Paulus DH, Braun H, Aklan B, Quick HH. Simultaneous PET/MR Hybrid Imaging : MR-based Attenuation Correction of Flexible Radiofrequency Surface Coils. Med Phys. 2012;39(7):4306–15. https://doi.org/10.1118/1.4729716.
[51] Delso G, Martinez-Möller A, Bundschuh RA, Nekolla SG, Ziegler SI. The effect of limited MR field of view in MR/PET attenuation correction. Med Phys 2010;37:2804–12. https://doi.org/10.1118/1.3431576.
[52] Tropp J. Image brightening in samples of high dielectric constant. J Magn Reson 2004;167:12–24. https://doi.org/10.1016/j.jmr.2003.11.003.
[53] Heußer T, Mann P, Rank CM, Scha M, Dimitrakopoulou-strauss A, Schlemmer H, et al. Investigation of the halo-artifact in 68 Ga-PSMA-11-PET/MRI. PLoS ONE 2017:1–19.
[54] Karlberg AM, Sæther O, Eikenes L, Goa PE. Quantitative comparison of PET performance—siemens biograph mCT and mMR. EJNMMI Phys 2016;3. https://doi.org/10.1186/s40658-016-0142-7.